

PAPER • OPEN ACCESS

## Scalable electromagnetic energy harvester for wind turbine rotor blade applications

To cite this article: Matthias Schlögl *et al* 2024 *Smart Mater. Struct.* **33** 055037

View the [article online](#) for updates and enhancements.

You may also like

- [Non-contact test set-up for aeroelasticity in a rotating turbomachine combining a novel acoustic excitation system with tip-timing](#)  
O Freund, M Montgomery, M Mittelbach et al.
- [Fibre-optic measurement of strain and shape on a helicopter rotor blade during a ground run: 1. Measurement of strain](#)  
Stephen W James, Thomas Kissinger, Simone Weber et al.
- [Diagnostics for piezoelectric transducers under cyclic loads deployed for structural health monitoring applications](#)  
Stuart G Taylor, Gyuhae Park, Kevin M Farinholt et al.



**ECS**  
The  
Electrochemical  
Society  
Advancing solid state &  
electrochemical science & technology

**DISCOVER**  
how sustainability  
intersects with  
electrochemistry & solid  
state science research

# Scalable electromagnetic energy harvester for wind turbine rotor blade applications

Matthias Schlögl\* , Michael Schneider  and Ulrich Schmid 

Institute of Sensor and Actuator Systems, TU Wien, Gußhausstraße 27-29, 1040 Vienna, Austria

E-mail: [matthias.schloegl@tuwien.ac.at](mailto:matthias.schloegl@tuwien.ac.at)

Received 15 January 2024, revised 8 March 2024

Accepted for publication 12 April 2024

Published 18 April 2024



CrossMark

## Abstract

One of the biggest challenges in structural health monitoring for rotor blades in wind turbines is to provide enough energy to power wireless sensor nodes. Batteries are not an adequate solution due to their limited lifetime and conventional cabling fails due to the rotation of the rotor blade. Therefore, we present an electromagnetic energy harvester that is specifically designed to be operated inside rotor blades and can generate a sufficient amount of energy. It uses the changing gravitational force vector to move a permanent magnet in a tube and converts this mechanical into electrical energy by coils arranged around the tube. Finite element methods simulations were performed to estimate the generated energy and an extensive parameter sweep of several key design parameters provided guidance for an optimized performance of a prototype. This device was characterized in the lab followed by a field test in a wind turbine where it was operated for several days and provided a continuous and rectified power of 6 mW, enough to power conventional wireless accelerometers, typically used within a predictive maintenance concept for the vibrational monitoring of rotor blades.

Keywords: energy harvester, electromagnetic, wireless sensor node, rotor blade, wind turbine

## 1. Introduction

The request for sustainable energy sources has led to the rapid growth of wind energy as a viable alternative to conventional power generation. Therefore, wind turbines have evolved significantly over the last years to harness wind energy more efficiently. In this context, the integration of wireless sensor networks within wind turbine rotor blades has emerged as a most promising approach for enabling predictive maintenance [1], monitoring structural health [2, 3], and for optimizing the overall output performance [4, 5]. However, powering these

sensors poses a particular challenge due to the remote and often inaccessible nature of turbine locations.

To address this challenge, typically two types of energy harvester designs are investigated: resonant and rotational energy harvesters. Resonant sensors usually use cantilever like structures which are tuned so that their resonances match the occurring frequencies of the underlying vibrating structure [6, 7]. Considering that every rotor blade has a unique vibrational spectrum which changes due to aging, wear or accidental events like lightning or icing [8–11], the use of resonant energy harvesters, which usually have a very limited bandwidth, is very challenging. Therefore, rotational energy harvesters seem more versatile and better suited for this task.

The energy of a rotational movement cannot be directly used and must be converted into another form. One way is to convert the low frequencies into higher frequencies, also known as frequency up-conversion, and excite a resonator at these higher frequencies. The resonator converts the

\* Author to whom any correspondence should be addressed.



Original content from this work may be used under the terms of the [Creative Commons Attribution 4.0 licence](https://creativecommons.org/licenses/by/4.0/). Any further distribution of this work must maintain attribution to the author(s) and the title of the work, journal citation and DOI.

kinetic into electric energy using either piezoelectric [12–15] or electromagnetic [16–19] transduction. Other researchers tried to convert the rotational into a linear motion and then use a combination of magnets and coils to generate electrical energy [20, 21].

However, most of these energy harvester designs are tailored to the specific requests of the targeted application and it is difficult to transfer a given harvester design to other applications. Especially, the conditions such as very low rotational frequencies or high centrifugal forces present in the inside of the rotor blades of wind turbines make it difficult to find suitable designs. Together with the need for power generation of several tens or hundreds of milliwatts to power a wireless sensor node as shown in this study, an energy harvester is requested fulfilling all these requirements.

In this paper we propose a sophisticated design of an electromagnetic energy harvester which is easily scalable in terms of energy generation. The paper is structured as follows: section 2 delves into the design considerations for an electromagnetic energy harvester tailored to wind turbine rotor blades. Section 3 analysis the performance and characteristics of our design by FEM simulations. Section 4 presents the experimental setup of the proposed energy harvester. Finally, in section 5 the energy harvester prototype is characterized first in lab and then under real-world conditions and comparisons of the results are made.

## 2. Energy harvester design considerations

The first step in designing the energy harvester was to estimate the amount of energy it has to produce. Therefore, the characteristics of commercially available sensor nodes was researched. Table 1 gives an overview of several commercially available autonomous accelerometer systems, used for vibrational condition monitoring.

For such continuously measuring battery-powered sensor nodes, the up-time depends on the sampling rate and on the transmission power resulting in values between 50 and 6000 h. To get a better understanding, the power consumption  $P_c$  of a G-Link-200 sensor node was measured as a function of sample rate and transmission power  $P_t$ , shown in figures 1(a) and (b), respectively. Depending on the targeted bandwidth of the vibrational spectra to be measured, the power draw reaches up to 50 mW for a transmission power of 0 dBm.

When harvesting energy in a rotor blade, one must consider that each rotor blade has its own characteristics in terms of e.g. vibrational frequency spectrum, size or rotational velocity. This makes it difficult to design an energy harvester working under these different conditions. However, one commonality inside a rotor blade of all wind turbines is, that the gravitational force acting on an object changes its direction periodically, depicted in figures 2(a) and (b). This boundary condition was taken as the basis for the design and the hardware development of the energy harvester.

The core element of the EMHE is a permanent magnet (PM) which is accelerated by the slowly rotating force vector (gravitation)  $F_G$ , whereas the trajectory of the PM is restricted to a linear movement by a guiding tube. This guiding tube is located tangential to the rotation circumference (see figure 2(c)). One or several coils are wound around the guiding tube, which convert the changing magnetic field caused by the moving PM into electric energy via Faraday's law of induction.

The mounting direction of the guiding tube is an important detail. It must be perpendicular to the direction of the centrifugal force  $F_{CF}$ . Otherwise, the magnet would get pulled into the direction of  $F_{CF}$  and stay there, as  $F_{CF}$  exceeds the gravitational force when mounting the harvester further away from the center. The exact distance depends on the rotational speed and can be estimated with  $r = g_0/\omega^2$ , whereas  $\omega^2$  is the angular velocity of the harvester and  $g_0$  is the gravitational constant.

## 3. Finite element methods model

To estimate the generated output characteristics and the influence of various coil circuit designs, finite element method simulations were performed with COMSOL Multiphysics 5.5. To reduce the simulation time, a simplified 2-dimensional axisymmetric model was implemented which can be seen in figure 3. It consists of the PM (1), several coils (2), and two separated regions—one surrounding the magnet and its possible trajectory (3), the other one surrounding the coils (4). The symmetry axis (5) is marked in red.

The movement of the PM was realized by a time-dependent study combined with a moving mesh, provided by COMSOL. The area (3) was set to free deformation, and a prescribed mesh displacement  $d_z$  in  $z$ -direction was applied to the magnet given by equation (3-1), representing the acceleration due to Gravitation,

$$d_z = -1/2\sqrt{g_0t^2f} \quad (3-1)$$

whereas  $g_0$  is the gravitational constant with a value of  $9.8067 \text{ ms}^{-2}$  and  $f$  is an experimentally evaluated dimensionless factor representing the frictional forces between the PM and the tube wall. The time-dependent study was set to a range of 0 – 0.6 s, with time steps of 0.0001 s and a relative solution tolerance of 0.0001. Each coil was linked with an *external voltage source* within the *electric circuit component* representing the induction voltage. The exact circuitry and device variations are described in the results section. A resistor equaling the inner coil resistance was connected as load to adjust for maximal generated power. As the load resistor value has to be defined before running the simulation, and the coil resistance is only simulated during simulation a precalculated resistance value was used, calculated by using equations (3-2)–(3-5) for a coil with  $n = 1$  and  $m = 1, 2, \dots, 4$  windings, according to figure 3(b)

**Table 1.** Specifications of exemplary commercially available sensor nodes.

Name	Sampling rate Hz	ADC bit	Transmission range m	Battery life	Transmission protocol	Measurement type
VibeSense	500–4000	16	Up to 30	Up to 80 h	Bluetooth	Continuous
G-Link-200	1–4096	20	Up to 2000	51–6000 h	LXRS	Continuous
ALTA	10–200	—	6096	22d@10 min, 266d@2 h	Proprietary	Heart beat
Fluke 3563	0–1000	24	100	365d@10 min	2.4 GHz ISM/IEEE 802.15.1	Heart beat

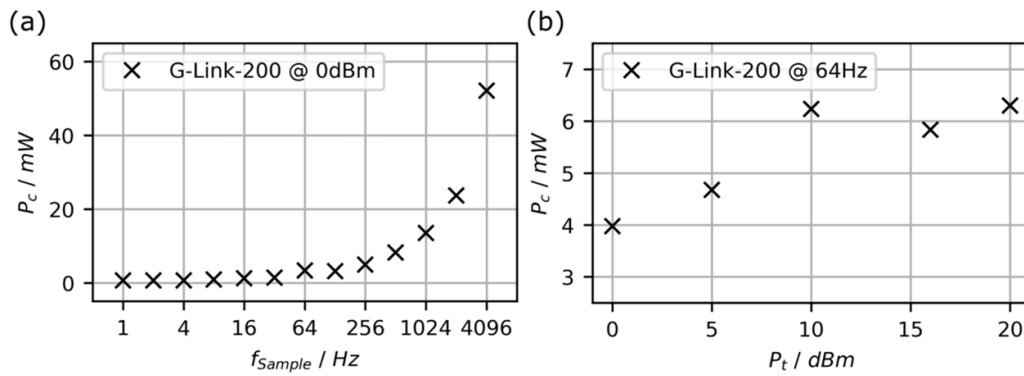


**Figure 1.** Power consumption of a LORD G-Link-200 as a function of (a) sample rate and (b) transmission power.

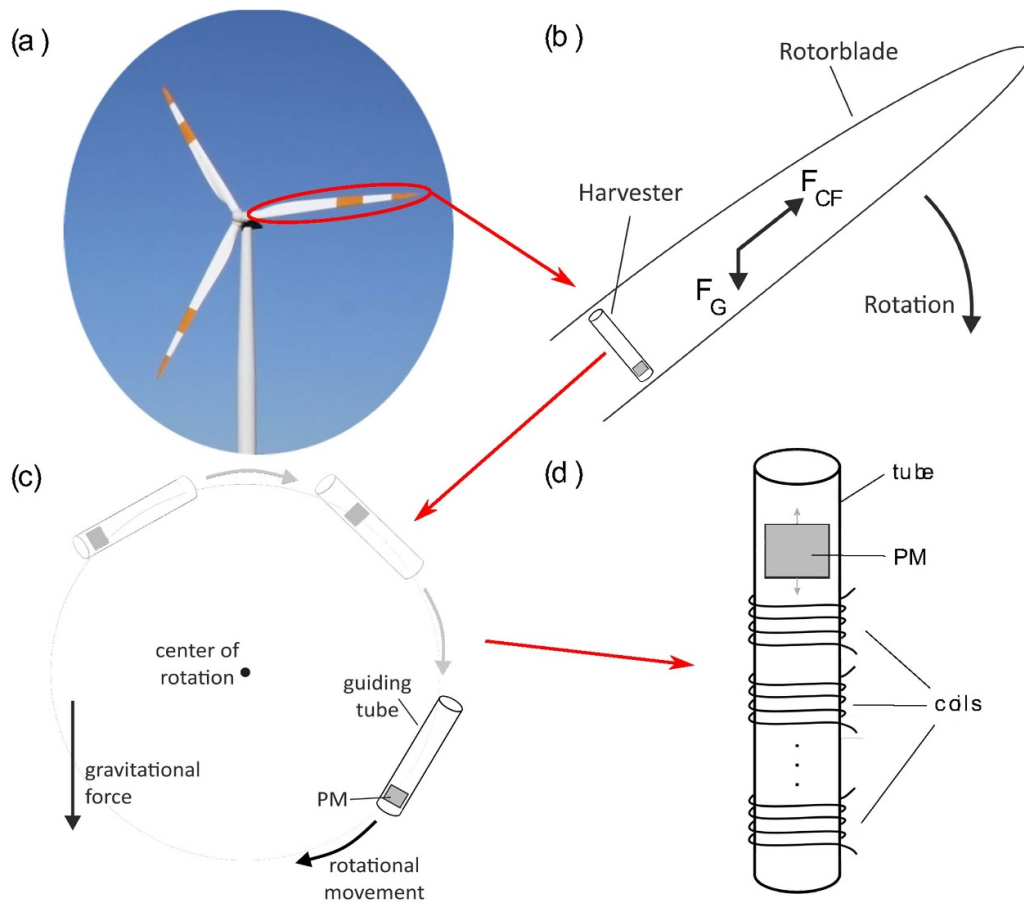


**Figure 2.** (a) Wind turbine with the marked rotor blade, where the energy harvester (EH) will be installed. (b) Alignment of the EH within the rotor blade. (c) Movement and forces acting on the EH from a point of view outside the rotor blade. (d) Detailed design of the EH.

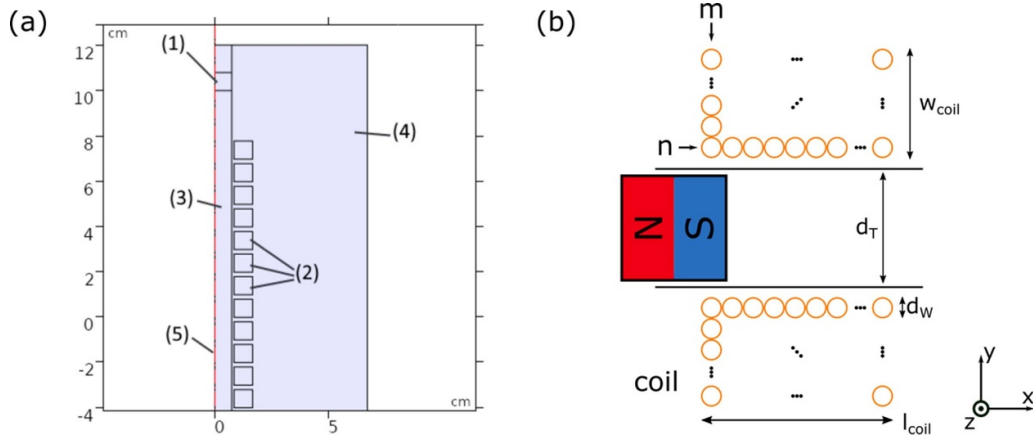


**Figure 3.** Simplified model of the energy harvester used for finite element method simulations.

$$R_{n=1,m=1} = \rho \left( \frac{2\pi \left( \frac{d_T}{2} + \frac{d_w}{2} \right)}{d_w^2 \pi / 4} \right) = 16\rho \left( \frac{1d_T}{d_w^2} + \frac{1}{d_w} \right) \quad (3-2)$$

$$\begin{aligned} R_{n=1,m=2} &= R_{n=1,m=1} + \rho \left( \frac{2\pi \left( \frac{d_T}{2} + \frac{3d_w}{2} \right)}{d_w^2 \pi / 4} \right) \\ &= 16\rho N \left( \frac{2d_T}{d_w^2} + \frac{4}{d_w} \right) \end{aligned} \quad (3-3)$$

$$\begin{aligned} R_{n=1,m=3} &= R_{n=1,m=2} + \rho \left( \frac{2\pi \left( \frac{d_T}{2} + \frac{5d_w}{2} \right)}{d_w^2 \pi / 4} \right) \\ &= 16\rho N \left( \frac{3d_T}{d_w^2} + \frac{9}{d_w} \right). \end{aligned} \quad (3-4)$$

The overall coil resistance was finally calculated by the expression:

$$R_{n=N,m=M} = 16\rho N \left( \frac{Md_T}{d_w^2} + \frac{M^2}{d_w} \right). \quad (3-5)$$

With  $N$  being the number of windings in  $x$ -direction and  $M$  being the number of windings in  $y$ -direction,  $\rho$  is the resistivity of copper,  $d_w$  is the wire diameter and  $d_t$  is the tube diameter, all shown in figure 3(b). This estimation presents a conservative way to calculate the coils resistance. More sophisticated methods, including random or helical winding can be found in [22].

#### 4. Experimental details

The main parts of the EH prototype are shown in figure 4. The tube and the endcaps were fabricated by a 3D printer of the type Prusa MK3S with an RS Pro polylactic acid filament. The PM was a combination of several commercially available NdFeB magnets. The coils were fabricated with a self-made coil winding machine and an isolated copper coil wire. To

soften the fall of the PM, end magnets were fixed into the end-cap, whereas the magnetic field of the end caps was opposing the field of the PM. The exact dimensions of the single parts can be found in table 2 at the end of this section. A detailed discussion about the PM magnet configuration and the coil number and circuitry can be found in the results section.

The prototype consists of two tubes with two PM and 18 coils on one tube and 12 coils on the other. The coil was created with a coil winding machine to the exact length and winding number obtained by the FEM simulations. All details of the coil can be found in table 2. The parts were fixed onto a wooden plate which then was glued into the rotor blade. The read out was realized by a Raspberry Pi 3 with a data acquisition board MCC118 DAQ from MC Measurement Computing, connected to a  $15 \times 3000$  mAh 18 650 Li-Ion batteries for standalone measurements in a rotor blade, shown in figure 5. The output of the energy harvester was connected to a conventional bridge rectifier and subsequently to an optimized load resistor. The determination of the load resistor can be found in chapter The DAQ board measured the voltage of the load resistor which then was used to calculate the generated energy  $E$  by using equation (4-1),

$$E = \int \frac{V_R(t)^2}{R} dt \quad (4-1)$$

## 5. Results and discussion

First, the output voltage and energy of a single coil with a single PM as a function of coil width and coil lengths are characterized, followed by a discussion about different types of multicoil interconnections and a combination of two magnets. The last part of this section describes a prototype, which was first characterized in the lab and then mounted into a real-world wind turbine, where its output voltage and generated energy were measured.

### 5.1. Coil dimensions

To optimize the generated power of a coil, its output voltage, generated energy per fall of the PM and the number of turns

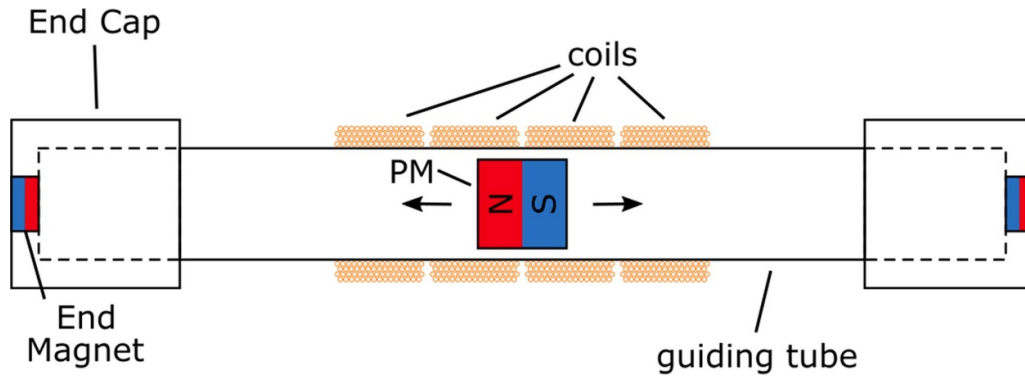


Figure 4. Design and single parts of the energy harvester prototype.

Table 2. Dimensions of all single parts of the energy harvester.

Coil width	$w_{\text{coil}}$	7 mm
Coil length	$l_{\text{coil}}$	8 mm
Coil number	$x$	18 + 12
Coil Resistance	$R_{\text{coil}}$	189 $\Omega$
Coil wire diameter	$d_w$	0.2 mm
Winding number	$N_{\text{coil}}$	2600
Load Resistance	$R_L$	5800 $\Omega$
Magnetic field strength	$B_{\text{PM}}$	1 T
Magnet size	$l_{\text{PM}} \times w_{\text{PM}} \times h_{\text{PM}}$	15 $\times$ 15 $\times$ 8 mm <sup>3</sup>
Tube length	$l_{\text{tube}}$	200 mm <sup>3</sup>

coil size, a FEM simulation with the model described above was used with only one coil and a PM with a length of 8 mm and a diameter of 15 mm.

Figure 6(a) shows the output voltage characteristics of a coil with varying width. While the voltage continuously increases the generated energies have a maximum at a coil width of 7 mm, as can be seen in figure 6(c), which depicts the generated energy and the according number of coil turns. This can be explained by the decreasing magnetic field strength for larger radii. At the same time the coils resistance increases with each turn, whereas outer turns add more resistance due to its higher radius.

Similar observations can be made when varying the coil length, where the optimum for generating energy is around 16 mm, shown in figure 6(b). In longer coils the magnetic field lines of the PM do not surround the whole coil and therefore, less voltage is induced. Similar to the change in width, longer coils also increase their resistance with each turn, which leads to an optimum for the generated energy at a length of 16 mm, shown in figure 6(d).

## 5.2. Magnet configurations and coil circuitry

This section studies the effect of combining several magnets and interconnecting several coils to increase the generated energy. A combination of several magnets of equal length in series, as depicted in figure 7(b), does increase the generated output energy compared to a single magnet, due to the higher magnetic field strength, especially when the coil length is adapted to the length of the PM. However, an even higher increase can be reached by combining two magnets in anti-series, where equally polarized ends are placed towards each other. Due to the strong repelling forces, a spacer with a length of 22 mm was used, as shown in figure 7(c).

Additional to the magnet configuration, a single coil can be replaced by a dual (or more) coil circuitry whereas the length, distance and polarization of the coils are adapted to the distance between the two magnets, shown in figures 8(b) and (c). The interconnections can be done in two ways—serial and anti-serial, as shown in figures 8(a)–(c).

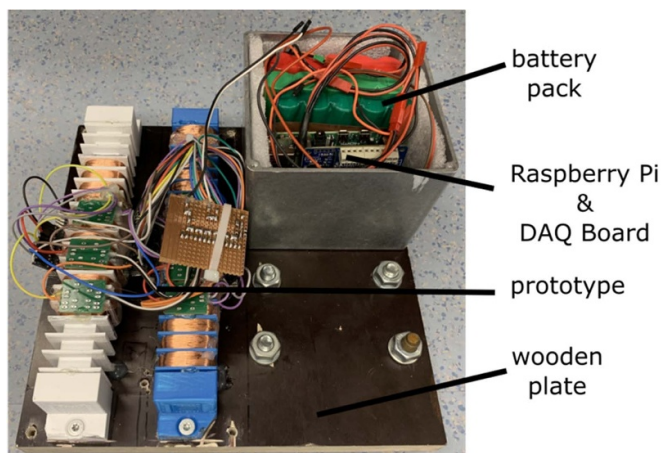
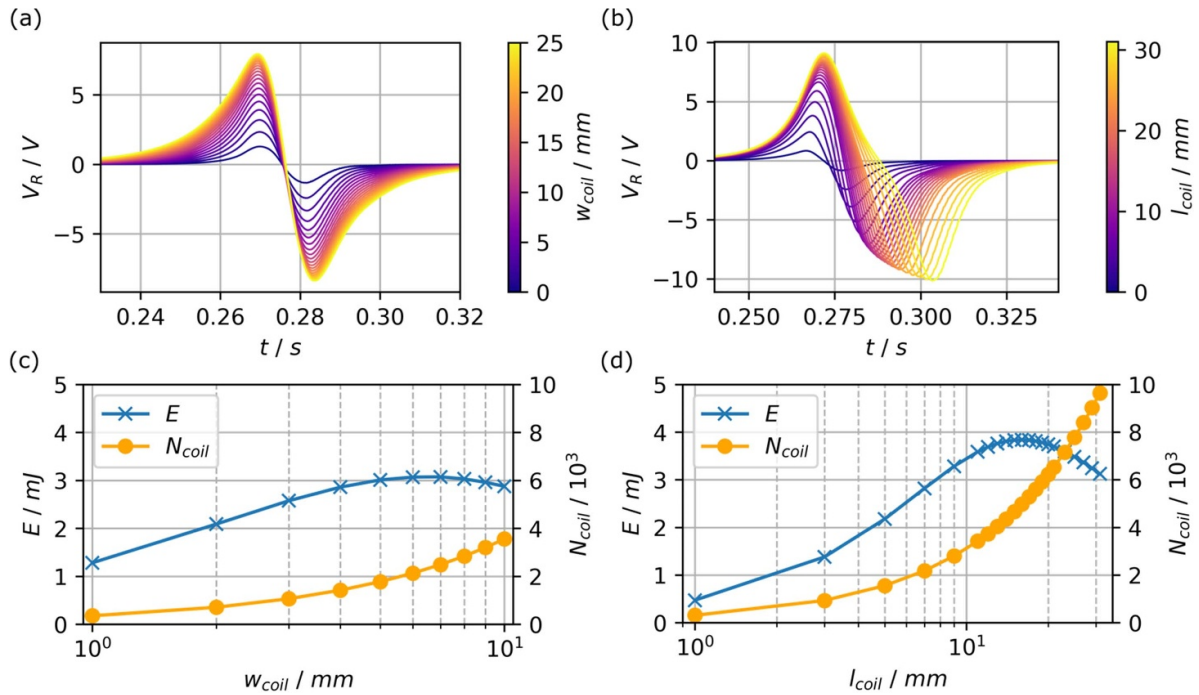
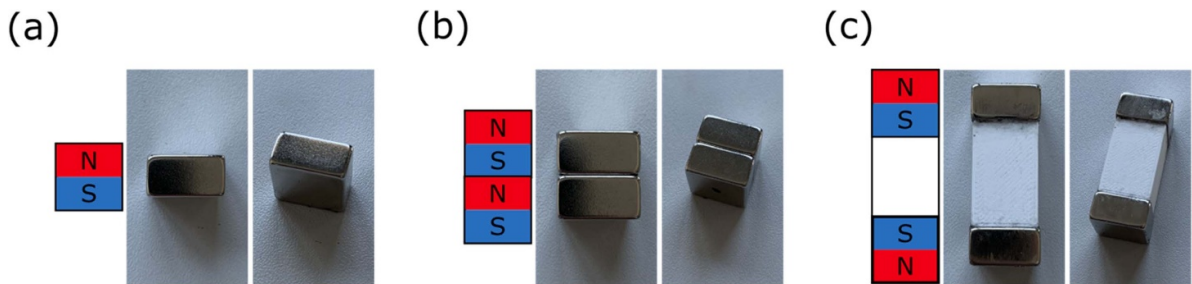


Figure 5. Photograph of the prototype indicating its main components and mounted on a base plate having dimensions of 25  $\times$  25 cm<sup>2</sup>.

were studied by varying the coils length and width. Generally, a higher number of windings leads to higher induction voltages and up to a certain limit also increases the generated output power. However, two effects counteract the increase in power. First, the coil resistance increases with more coil turns, and with the larger radius, the outer turns also have a higher resistance per turn. Secondly, the magnetic stray field of the PM through the coil leads to lower induction voltage in the outer turns of the coil. To estimate the optimal number of turns and



**Figure 6.** Output voltage of a single coil with (a) varied width and (b) varied length and generated energy and coil windings as a function of (a) width and (b) length.



**Figure 7.** Different magnet configurations. (a) Single magnet with a size of  $15 \times 15 \times 8 \text{ mm}^2$ , (b) dual magnet and (c) dual anti-serial magnet with a spacer length of 22 mm<sup>2</sup> configuration.

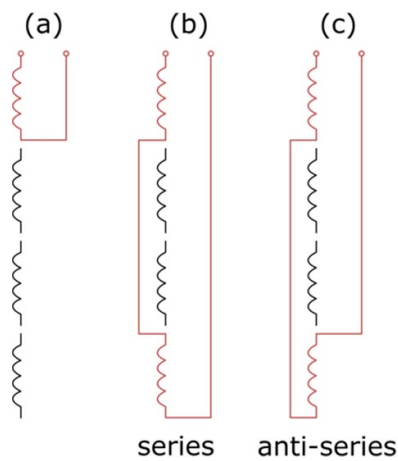


**Figure 8.** (a) Single coil and the two different coil interconnections (b) in series and (c) in anti-series for the dual anti-serial magnet configuration.

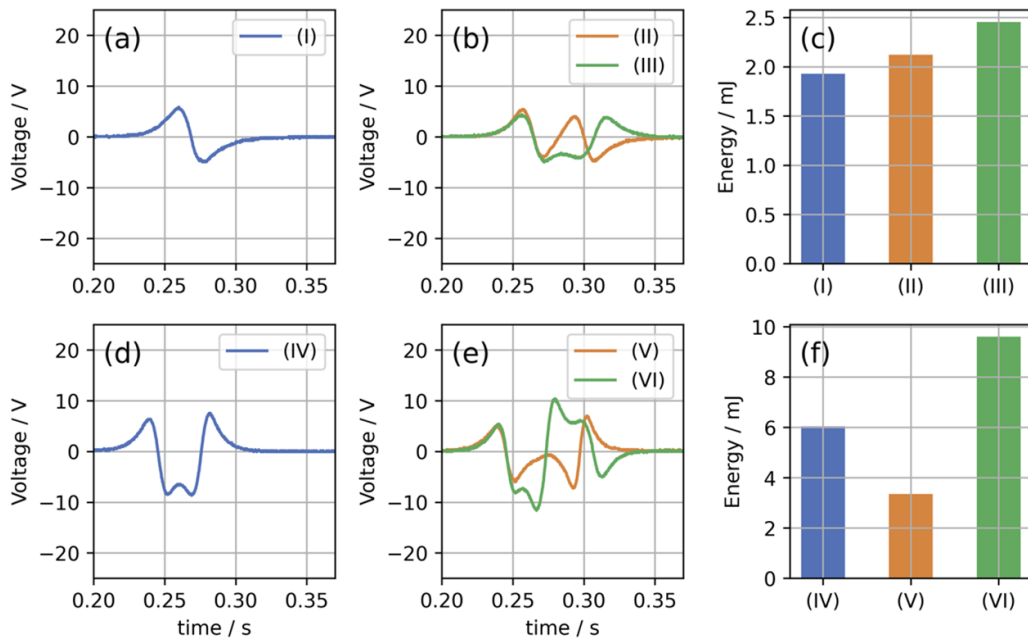


**Figure 9.** Generated output voltages and energies of a single magnet in (a)–(c) and a dual anti-serial magnet configuration in (d)–(f). In (a) and (d) the output voltage of a single coil and in (b) and (e).

Figures 9(a) and (b) show the induced voltages and (c) the corresponding generated energies for a single magnet. In (a) the magnet is moving through a single coil (I) and in (b) two coils are used interconnected in series (II) and in anti-series (III). The two-coil anti-series connection increases the energy from  $\sim 2$  mJ for the single coil to  $\sim 2.5$  mJ. Figures 9(d)–(f) show the same coil circuitries but for a dual anti-serial magnet configuration. In all three cases, the dual-magnets generated more energy, whereas in the case of a two-coil anti-series connection (VI) the energy output could be increased to  $\sim 9.5$  mW which corresponds to a 60% increase, compared to the single magnet, single coil configuration.

Other coil distances and interconnections are omitted here, as they generate less output energy due to the mutual cancellation of induced voltages.

Figures 10(a) and (b) show the simulated output voltages and energies as a function of coil length for the dual coil circuit in anti-series connection. Interestingly there are two maxima, one at a coil length of 8 mm with  $\sim 22$  mW and one at 20 mm with  $\sim 23$  mW. The minimum between the two maxima can be traced back to the mutual cancellation of the induced voltages of the two oppositely polarized magnets when they move through the coils connected in anti-series. While the longer coils generate more energy it also occupies more space along the tube. When combining several of those dual coil interconnections, then more coils can be placed along the tube which will be termed a multi-coil setup in this work. Therefore, for the prototype introduced in a later section, coils with a length of 8 mm are used.

To investigate such a multi-coil setup the COMSOL model was extended in several steps up to 18 coils as shown in figures 11(a)–(c) for the first three steps (3, 6 and 9 coils).

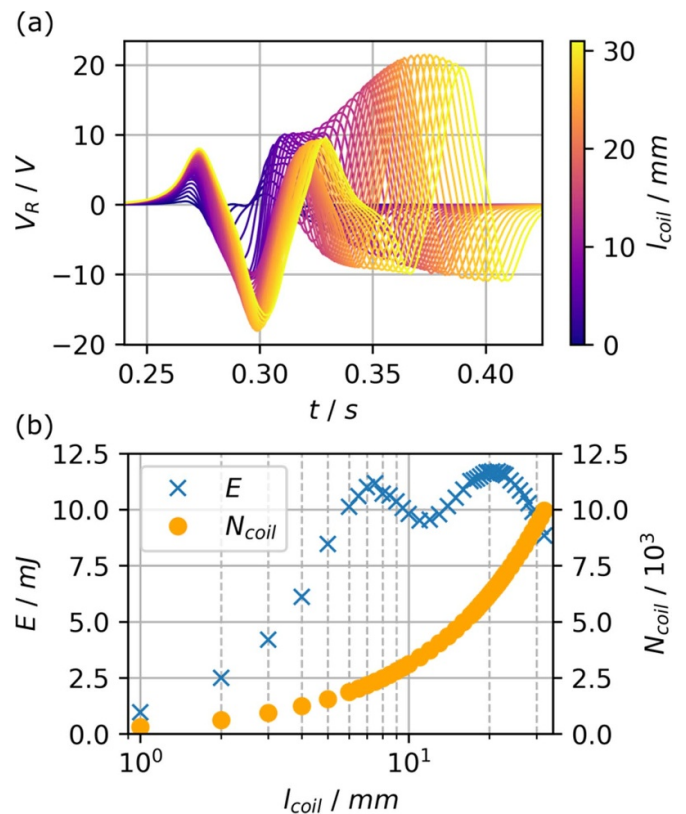


**Figure 10.** (a) Output voltage of a dual coil setup in anti-series connection for different coil lengths. (b) Generated energies and coil winding number as a function of coil length.

Figure 11(d) shows the generated output energies as a function of coil number. With each additional stage the total generated energy increases.

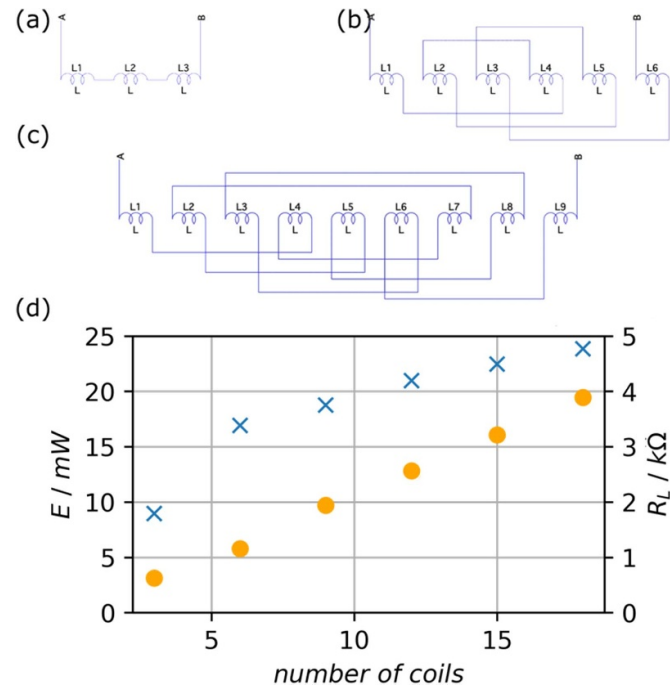


**Figure 11.** Circuitries for combination of (a) three, (b) six and (c) nine coils. (d) Generated energies and according load resistance as a function of number of coils for a multicoil setup.

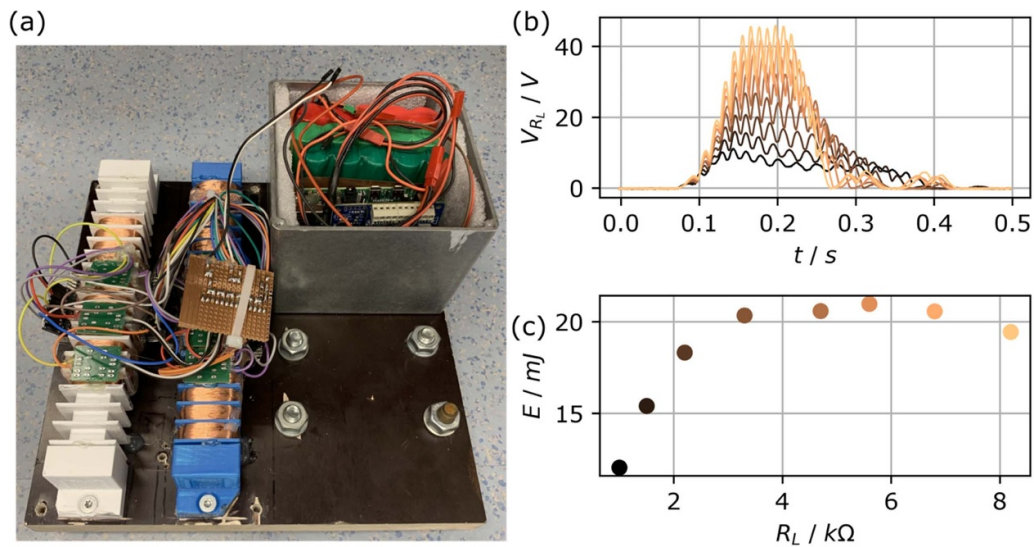


**Figure 12.** (a) Photograph of the prototype. (b) Output voltage of the prototype for different load resistor values. (c) Generated energy as a function of load resistor value.

### 5.3. Prototype characterization and field test in a wind turbine

Based on the results from the FEM simulations, an energy harvesting prototype was built, consisting of two tubes, two PMs, and 18 + 12 coils, as shown in figure 12(a). The readout circuit and rectification are described in section 4. The characterization in the lab was performed under optimized conditions, which means the tube was turned from a horizontal to a vertical position, fast enough so that the magnet would not start falling, before the tube was not in a completely vertical position. This

results in a nearly free fall of the magnet, where the frictional forces can be neglected. In the real-world scenario additional frictional forces come into play, which will be discussed in detail in section 5.4.

The optimal load resistance was determined by sweeping the load resistance value from 560Ω to 8200Ω. This confirms the theoretically predicted value of a series interconnection of all inner coil resistances resulting in  $R_L = 30 \cdot 189\Omega + R_{\text{rect}} \approx 5.8 \text{ k}\Omega$  with  $R_{\text{rect}}$  representing the inner resistance of the rectifier. Figure 12(b) shows the voltages at the load resistance for different resistance values and (c) shows

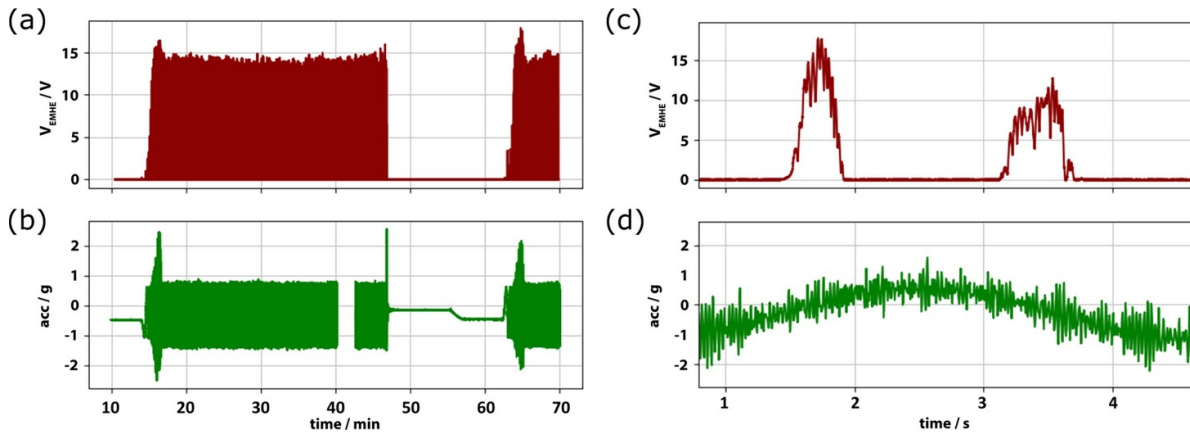


**Figure 13.** Output voltage (in red) and measured accelerations (in green) of the prototype placed in the wind turbine for a time duration of (a), (b) one hour and (c), (d) five seconds.

the accordingly generated energies as a function of the load resistance.

The prototype was then taken to a real wind turbine and installed in one of the rotor blades next to an acceleration sensor of the type Lord G-Link 200. Figures 13(a) and (b) show the output voltage of the EH in red and the acceleration along the blade length measured by an accelerometer installed next to the EH in green. A representative time frame of one hour is presented, where a startup followed by an emergency stop (for testing purposes) and another startup, occurred. Figures 13(c) and (d) show one rotation of the rotor blade with two double peaks. While the peak shape is similar to the one measured in the lab, the peak duration is 2.5 times as long and the peak voltage is half of the peak voltage measured in the lab. The reason for this will be discussed in the next section.

#### 5.4. Comparison

The electromagnetic energy harvester generated on average 6 mW at a peak voltage of 15 V during operation in the wind turbine, whereas in the lab a peak voltage of 40 V and an energy of 38 mJ per fall of the magnet was generated. This translates to an average power generation of 25 mW if considering that the EH is used in a wind turbine with a rotational frequency of 20 rpm. The reason for this difference is twofold. First, the rotational frequency of the test turbine was 16 rpm—a bit lower than the assumed 20 rpm. Second, the velocity of the PM is reduced, due to frictional forces generated through the slowly rotating guiding tube and the additional centrifugal force. In contrast, the guiding tube in the lab is placed vertically, which minimizes the friction between the tube wall and the falling magnet. Figure 14 shows the movement of the PM and the tube in the lab compared to the movement in the rotor blade. In the lab, the PM falls in a direct line from top to bottom, accelerated constantly with 1 g with negligible impact

from friction, whereas in the rotor blade, the tube is slowly turned from a horizontal into a vertical position. This creates additional friction for the PM while accelerating, resulting in a reduced acceleration and speed and hence, a reduced induced voltage. The generated energy goes with the square of the induced voltage, which explains the large difference in both values.

Another question arising is how much energy could theoretically be harvested under optimal conditions. For this the potential energy of the PM can be calculated by equation (5.4-1),

$$E_{\text{pot}} = m_{\text{PM}} \cdot g_0 \cdot h. \quad (5.4-1)$$

With the values for all terms given in table 3 the potential energy can be calculated to  $E_{\text{pot}} \approx 60$  mJ. Compared to the potential energy, the measurements in the lab and in the wind turbine result in an efficiency of 63% and 15%, respectively. These differences are most likely originating from additional friction between the PM and the tube wall as explained before.

To compare this design of an energy harvester to other similar designs the normalized power density  $p_{\text{NPD}}$  can be used which relates the generated power to its volume. In this case the volume is approximated by a rectangularly shaped box surrounding the outer edges of the EH. Another important characteristic property is the frequency at which the EH is operated. Considering that the peak is approximately 0.2 s (compare figure 14) long the peaks can occur with a frequency of 5 Hz at which the generated power calculates to 110 mW and  $p_{\text{NPD,IB}} = 373.75 \mu\text{W cm}^{-2}$ . In figure 15  $p_{\text{NPD}}$  is plotted as a function of frequency and compared with state-of-the-art EHs from table 4. In the plot, the transduction principle is indicated by colors, whereas green is for piezoelectric, blue is for electromagnetic and purple is for a combination of both. Additionally, the shape of the marker indicates the actuation mechanism, where triangles indicate a continuous actuation

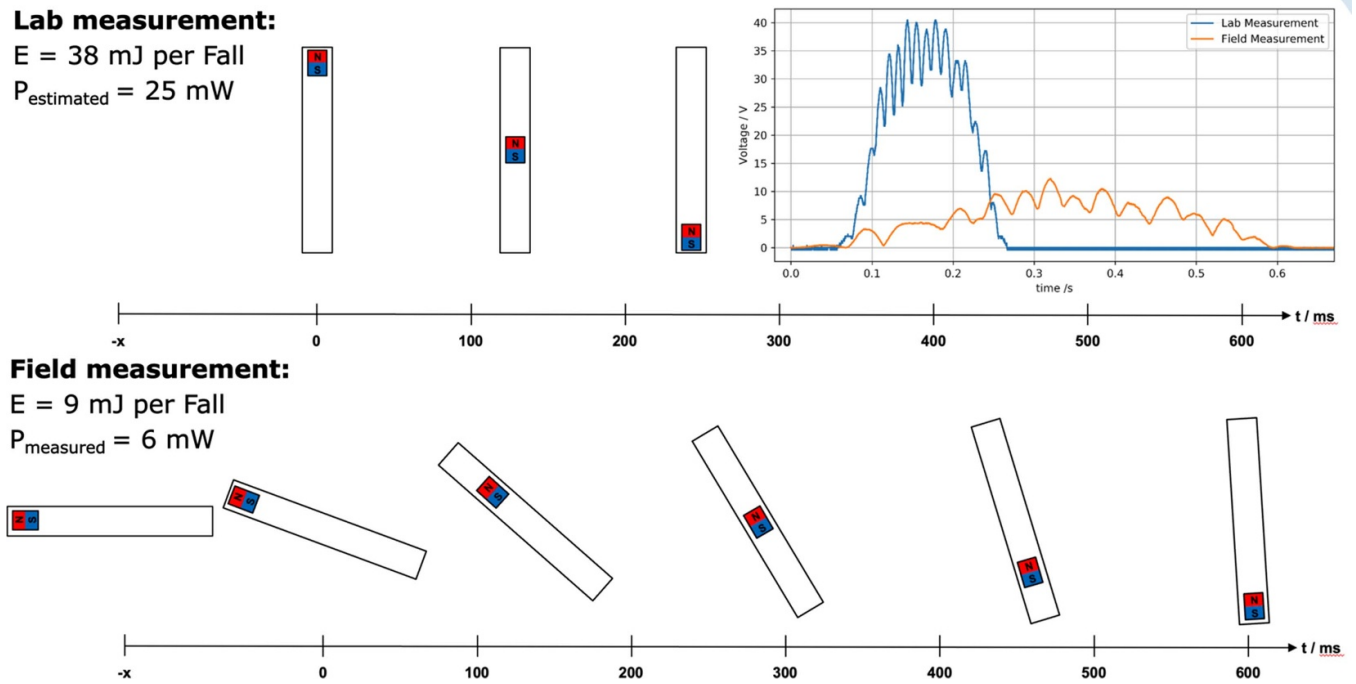


**Figure 14.** Comparison of the movement of the guiding tube and the PM between lab- and field-measurements.

**Table 3.** Dimensions of important components of the energy harvester as well as the gravitational acceleration.

Mass of PM	$m_{\text{PM}}$	30 g
Gravitation	$g_0$	$9.81 \text{ m s}^{-2}$
Tube height	$h$	20 cm
Potential Energy of PM	$E_{\text{pot}}$	60 mJ
Energy generated in lab	$E_{\text{lab}}$	38 mJ
Energy generated in wind turbine	$E_{\text{wt}}$	9 mJ

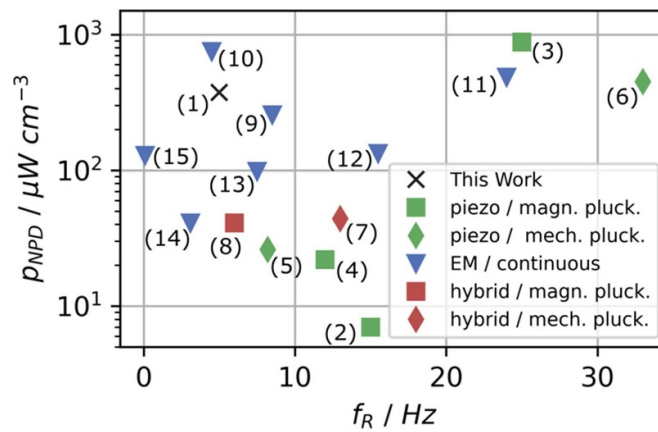


**Figure 15.** Normalized power density as a function of frequency of various state-of-the-art energy harvesters with an electromagnetic or piezoelectric transduction mechanism.

and squares and diamonds relate to a magnetic and a mechanical plucking mechanism, respectively. The plot shows that electromagnetic non-resonant designs perform better under low-frequency conditions, whereas piezoelectric harvesters

show higher normalized power densities at higher frequencies. However, it must be noted that while they appear similar, our EH is the only one specially designed for use in the rotor blade of a wind turbine.

**Table 4.** Overview of various state-of-the-art energy harvesters with an electromagnetic or piezoelectric transduction mechanism.

Nr.	Author	Year	Transduction mechanism	$p_{\text{NPD}} \mu\text{W cm}^{-3}$	$p \mu\text{W}$	$f_R \text{Hz}$	Actuation principle	References
1	This work	2023	EM	374	6000	5	Continuous	—
2	Tang et al	2011	Piezo	7	22.5	15	Magnetic plucking	[23]
3	Wu et al	2017	Piezo	878	1230	25	Magnetic plucking	[24]
4	Fakeih et al	2021	Piezo	22	38	12	Magnetic plucking	[25]
5	Gu and Livermore	2011	Piezo	26	429	8.2	Mechanical plucking	[26]
6	Jung et al	2013	Piezo	450	—	33	Mechanical plucking	[27]
7	Wang et al	2020	Piezo	478	78 870	34	Mechanical plucking	[28]
7	Xu et al	2017	Piezo/EM	44	769	13	Mechanical plucking	[29]
8	Fan et al	2018	Piezo/EM	41	1500	6	Magnetic plucking	[30]
9	Luo et al	2017	EM	256	—	8.5	Continuous	[31]
10	Shen and Lu	2020	EM	748	—	4.5	Continuous	[32]
11	Li et al	2019	EM	484	—	24	Continuous	[33]
12	Nammari et al	2018	EM	133	—	15.5	Continuous	[34]
13	Fan et al	2019	EM	98	—	7.5	Continuous	[35]
14	Zhang et al	2019	EM	41	—	3.1	Continuous	[36]
15	Luo et al	2020	EM	129	—	0.1	Continuous	[37]

## 6. Conclusion and outlook

In this work, an energy harvester concept specifically designed to power wireless sensor networks for the use inside a rotor blade of a wind turbine is presented. Next, the device is realized in hardware and evaluated both under lab conditions and at real wind turbines. Additionally, extensive finite element methods simulations with COMSOL were performed in advance to estimate the optimized dimensions between the PM and the coils. The prototype of the energy harvester provided 38 mJ of energy per fall of the PM during characterization in the lab which would calculate to a continuous 25 mW of power inside a rotor blade rotating with 20 rpm. During the field test in a real-world wind turbine, however, the energy harvester could generate only an average power of 6 mW. The reason for this difference could be found in the additional friction due to the slowly rotating rotor blade. The normalized power density of the harvester was calculated to  $374 \mu\text{W cm}^{-3}$  which is comparable to other state-of-the-art harvesters. All in all, the successful operation of electromagnetic energy harvesters could be demonstrated at wind turbines, paving the way for wireless sensor nodes enabling a continuous monitoring and hence, predictive maintenance of rotor blades.

### Data availability statement

The data cannot be made publicly available upon publication because they are not available in a format that is sufficiently accessible or reusable by other researchers. The data that support the findings of this study are available upon reasonable request from the authors.

### Acknowledgments

We greatly acknowledge the financial support by the FFG under Contract Number 865960/2018.

The authors acknowledge TU Wien Bibliothek for financial support through its Open Access Funding Program.

### ORCID iDs

Matthias Schlögl  <https://orcid.org/0000-0003-1226-6570>

Michael Schneider  <https://orcid.org/0000-0001-9846-7132>

Ulrich Schmid  <https://orcid.org/0000-0003-4528-8653>

### References

- [1] Gong L and Chen Y 2024 Machine learning-enhanced IoT and wireless sensor networks for predictive analysis and maintenance in wind turbine systems *Int. J. Intell. Netw.* **5** 133–144
- [2] Le T-C, Luu T-H-T, Nguyen H-P, Nguyen T-H, Ho D-D and Huynh T-C 2022 Piezoelectric impedance-based structural health monitoring of wind turbine structures: current status and future perspectives *Energies* **15** 15
- [3] Kim H-G and Kim J-Y 2021 Analysis of wind turbine aging through operation data calibrated by LiDAR measurement *Energies* **14** 8
- [4] Wagner R, Pedersen T F, Courtney M, Antoniou I, Davoust S and Rivera R L 2014 Power curve measurement with a nacelle mounted lidar *Wind Energy* **17** 1441–53
- [5] Theuer F, van Dooren M F, von Bremen L and Kühn M 2020 Minute-scale power forecast of offshore wind turbines using long-range single-Doppler lidar measurements *Wind Energy Sci.* **5** 1449–68
- [6] Yang Z, Zhou S, Zu J and Inman D 2018 High-performance piezoelectric energy harvesters and their applications *Joule* **2** 642–97
- [7] Raghavan S, Gupta R and Sharma L 2023 Applications of a novel tunable piezoelectric vibration energy harvester *Micromachines* **14** 9
- [8] Wondra B, Malek S, Botz M, Glaser S D and Grosse C U 2019 Wireless high-resolution acceleration measurements for structural health monitoring of wind turbine towers *Data-Enabled Discov. Appl.* **3** 4
- [9] Kilic G and Unluturk M S 2015 Testing of wind turbine towers using wireless sensor network and accelerometer *Renew. Energy* **75** 318–25

- [10] Joshua A and Sugumaran V 2019 Improvement in wind energy production through condition monitoring of wind turbine blades using vibration signatures and ARMA features: a data-driven approach *Prog. Ind. Ecol. Int. J.* **13** 207–31
- [11] García D and Tcherniak D 2019 An experimental study on the data-driven structural health monitoring of large wind turbine blades using a single accelerometer and actuator *Mech. Syst. Signal Process.* **127** 102–19
- [12] Fang S, Chen K, Lai Z, Zhou S and Liao W-H 2023 Analysis and experiment of auxetic centrifugal softening impact energy harvesting from ultra-low-frequency rotational excitations *Appl. Energy* **331** 120355
- [13] Nezami S, Jung H and Lee S 2019 Design of a disk-swing driven piezoelectric energy harvester for slow rotary system application *Smart Mater. Struct.* **28** 074001
- [14] Fang S, Wang S, Zhou S, Yang Z and Liao W-H 2020 Exploiting the advantages of the centrifugal softening effect in rotational impact energy harvesting *Appl. Phys. Lett.* **116** 063903
- [15] Townsend S, Grigg S, Picelli R, Featherston C and Kim H A 2019 Topology optimization of vibrational piezoelectric energy harvesters for structural health monitoring applications *J. Intell. Mater. Syst. Struct.* **30** 2894–907
- [16] Ahmad M M, Khan N M and Khan F U 2021 Review of frequency up-conversion vibration energy harvesters using impact and plucking mechanism *Int. J. Energy Res.* **45** 15609–45
- [17] Li X, Hu G, Guo Z, Wang J, Yang Y and Liang J 2022 Frequency up-conversion for vibration energy harvesting: a review *Symmetry* **14** 3
- [18] Pyo S, Kwon D-S, Ko H-J, Eun Y and Kim J 2022 Frequency up-conversion hybrid energy harvester combining piezoelectric and electromagnetic transduction mechanisms *Int. J. Precis. Eng. Manuf.-Green Technol.* **9** 241–51
- [19] Zorlu Ö, Topal E T and Külah H 2011 A vibration-based electromagnetic energy harvester using mechanical frequency up-conversion method *IEEE Sens. J.* **11** 481–8
- [20] Joyce B S, Farmer J and Inman D J 2014 Electromagnetic energy harvester for monitoring wind turbine blades *Wind Energy* **17** 869–76
- [21] Grundkötter E and Melbert J 2019 Energy self-sufficient wireless sensor node for inertial measurements on wind turbine blades *2019 IEEE Sensors* pp 1–4
- [22] Hagedorn J, Blanc F S-L and Fleischer J (eds) 2018 *Handbook of Coil Winding* (Springer) (<https://doi.org/10.1007/978-3-662-54402-0>)
- [23] Tang Q C, Yang Y L and Li X 2011 Bi-stable frequency up-conversion piezoelectric energy harvester driven by non-contact magnetic repulsion *Smart Mater. Struct.* **20** 125011
- [24] Wu W-H, Kuo K-C, Lin Y-H and Tsai Y-C 2018 Non-contact magnetic cantilever-type piezoelectric energy harvester for rotational mechanism *Microelectron. Eng.* **191** 16–19
- [25] Fakeih E, Almansouri A S, Kosel J, Younis M I and Salama K N 2021 A wideband magnetic frequency up-converter energy harvester *Adv. Eng. Mater.* **23** 2001364
- [26] Gu L and Livermore C 2011 Impact-driven, frequency up-converting coupled vibration energy harvesting device for low frequency operation *Smart Mater. Struct.* **20** 045004
- [27] Jung H J, Song D, Hong S K, Song Y and Sung T H 2013 Effective piezoelectric area for hitting-type piezoelectric energy harvesting system *Jpn. J. Appl. Phys.* **52** 10MB03
- [28] Wang Y, Yang Z, Li P, Cao D, Huang W and Inman D J 2020 Energy harvesting for jet engine monitoring *Nano Energy* **75** 104853
- [29] Xu Z, Wang W, Xie J, Xu Z, Zhou M and Yang H 2017 An impact-based frequency up-converting hybrid vibration energy harvester for low frequency application *Energies* **10** 11
- [30] Fan K, Liu S, Liu H, Zhu Y, Wang W and Zhang D 2018 Scavenging energy from ultra-low frequency mechanical excitations through a bi-directional hybrid energy harvester *Appl. Energy* **216** 8–20
- [31] Luo Q, He X, Jiang S and Wang X 2017 Impact-based electromagnetic energy harvester with high output voltage under low-level excitations *Energies* **10** 11
- [32] Shen Y and Lu K 2020 Scavenging power from ultra-low frequency and large amplitude vibration source through a new non-resonant electromagnetic energy harvester *Energy Convers. Manage.* **222** 113233
- [33] Li Z, Yan Z, Luo J and Yang Z 2019 Performance comparison of electromagnetic energy harvesters based on magnet arrays of alternating polarity and configuration *Energy Convers. Manage.* **179** 132–40
- [34] Nammari A, Caskey L, Negrete J and Bardaweel H 2018 Fabrication and characterization of non-resonant magneto-mechanical low-frequency vibration energy harvester *Mech. Syst. Signal Process.* **102** 298–311
- [35] Fan K, Zhang Y, Liu H, Cai M and Tan Q 2019 A nonlinear two-degree-of-freedom electromagnetic energy harvester for ultra-low frequency vibrations and human body motions *Renew. Energy* **138** 292–302
- [36] Zhang L B, Dai H L, Yang Y W and Wang L 2019 Design of high-efficiency electromagnetic energy harvester based on a rolling magnet *Energy Convers. Manage.* **185** 202–10
- [37] Luo A, Zhang Y, Dai X, Wang Y, Xu W, Lu Y, Wang M, Fan K and Wang F 2020 An inertial rotary energy harvester for vibrations at ultra-low frequency with high energy conversion efficiency *Appl. Energy* **279** 115762